Astron. Astrophys. 233, 96–111 (1990)

ASTRONOMY
AND
ASTROPHYSICS

Charge composition and energy spectra of cosmic-ray nuclei for elements from Be to Ni. Results from HEAO-3-C2

J.J. Engelmann[1], P. Ferrando[1], A. Soutoul[1], P. Goret[1], E. Juliusson[3], L. Koch-Miramond[1], N. Lund[2], P. Masse[1], B. Peters[2], N. Petrou[1], and I.L. Rasmussen[2]

[1] Service d'Astrophysique, CEN-Saclay, F-91191 Gif-sur-Yvette, France
[2] Danish Space Research Institute, Lundtoftevej 7, Lyngby, Denmark
[3] Science Institute, University of Iceland, IS-107 Reykjavik, Iceland

Received June 28, accepted November 6, 1989

Abstract. We give the final analysis of the data on the elemental cosmic ray composition from the French-Danish experiment onboard HEAO-3. The relative abundances of elements of charge 4 to 28 have been calculated for 14 energy windows extending from 0.6 to 35 GeV/n. By selecting those parts of the orbit where the telescope axis is nearly vertical, it has also been possible to draw from the data the absolute energy spectra of these elements. The rigidity dependence of the escape length of cosmic rays in the galaxy has been derived in the framework of the leaky box model from the measured values of the B/C ratio. Assuming the interstellar medium is composed of 90% H and 10% He, and using the most recently measured cross sections (Webber, 1989; Ferrando et al., 1988b), the escape length has been found equal to $34\beta R^{-0.6}$ g cm^{-2} for rigidities R above 4.4 GV, and 14β g cm^{-2} below. The source abundances were then derived from the observed values, and the results for the main primary elements are presented in this paper. The value found for the source N/O ratio, $4.8 \pm 1.7\%$, agrees within errors with the isotopic determinations at high and low energies. The source spectrum of all species is reasonably well fit by a power law in momentum, with a spectral index 2.23 ± 0.05, but only up to 16 GeV/n. This value is compatible with those found for H and He nuclei.

Key words: cosmic rays – abundances – energy spectrum

1. Introduction

The French-Danish Cosmic Ray experiment C2 was launched in 1979 onboard the NASA HEAO-3 satellite. It was initially designed to determine the mean masses of the most abundant elements in the galactic cosmic radiation at high energy. This goal was actually achieved, and has yielded the sole data available today about isotopic composition of cosmic rays above 2 GeV/n (Ferrando et al., 1988a; Herrstrom et al., 1985). Moreover, the large geometry of this experiment, combined with the good resolution of its various detectors, has also allowed to get important results in other fields. These include the measurements of the elemental composition and energy spectra of cosmic rays with an unprecedented accuracy in the ~1–35 GeV/n range (Koch et al., 1981; Engelmann et al., 1983, 1985; Juliusson et al., 1983; Byrnak et al., 1983), and the determination of an upper limit to the ratio of antinuclei to nuclei for particles with charge >9 (Lund and Rotenberg, 1985). From these results, the abundances and the energy spectra of the primary cosmic rays at their source were determined (Engelmann et al., 1983, 1985), giving important constraints to the models of cosmic ray sources and acceleration. Finally, the accurate secondary to primary ratios measured on HEAO3-C2, combined with a better knowledge of the fragmentation cross sections (Webber et al., 1987) and a better representation of the Interstellar Medium (Ferrando et al., 1988b; Soutoul and Ferrando, 1989), have provided new clues for the understanding of the cosmic ray propagation in the Galaxy.

In this paper, we present the final results of the HEAO-C2 data on the elemental composition of cosmic rays up to $Z=28$. We give a new table of elemental abundances and absolute energy spectra of cosmic ray nuclei with $Z=4$ to 28 in the 0.6–35 GeV/n range, as measured in 1980. The following important improvements have been achieved in this final analysis. First, better values were obtained for the efficiency of the hodoscope system, as a function of charge and energy. Second, the previous analysis of the C2 data did not include an estimate of the collection factor of the instrument, which prevented us from getting the absolute fluxes (the spectra presented by Engelmann et al. (1985) were arbitrarily normalized at 10 GeV/n to other available data). It has now been possible to derive a value for the collection factor of the instrument on selected parts of the orbit, so as to get absolute fluxes. Third, a better measurement of the momentum of the particles was achieved, and a simpler method was designed to get the cosmic ray spectra. Finally, periods with Forbush decreases have been excluded of the spectral analysis, in order to avoid transient distortions of the spectra and to make meaningful comparisons with other data obtained during solar minimum periods.

This paper is organized as follows. A description of the instrument with its characteristics is given in Sect. 2. Section 3 is specifically devoted to the data analysis procedure. Section 4 elaborates on the derivation of the elemental abundances. The absolute energy spectra are then presented in Sect. 5. In Sect. 6, a new table of Galactic Cosmic Ray Source abundances is given, as derived from our data in the Leaky-Box model using the most recent cross section data. The conclusions of this work are presented in Sect. 7.

Send offprint requests to: J.J. Engelmann

2. Instrumentation

2.1. Telescope assembly

A detailed description of the instrument has been published earlier by Bouffard et al. (1982). Here we restrict the presentation to the main characteristics of the experiment, whose configuration is illustrated in Fig. 1. It consists of five Cerenkov counters with different refractive indices and an hodoscope of four flash tube arrays inserted between the counters. Each array is made up of two perpendicular layers of 128 tubes each. The instrument being bidirectional, a time of flight measurement between top and bottom counters is used to identify the direction of propagation of the particle.

An event is accepted if counters C1, C3 and C5 are simultaneously triggered. Then the amplitude of the signals from the five counters, the addresses of the flash tubes fired and the value of the time of flight are encoded and transmitted to ground by the telemetry.

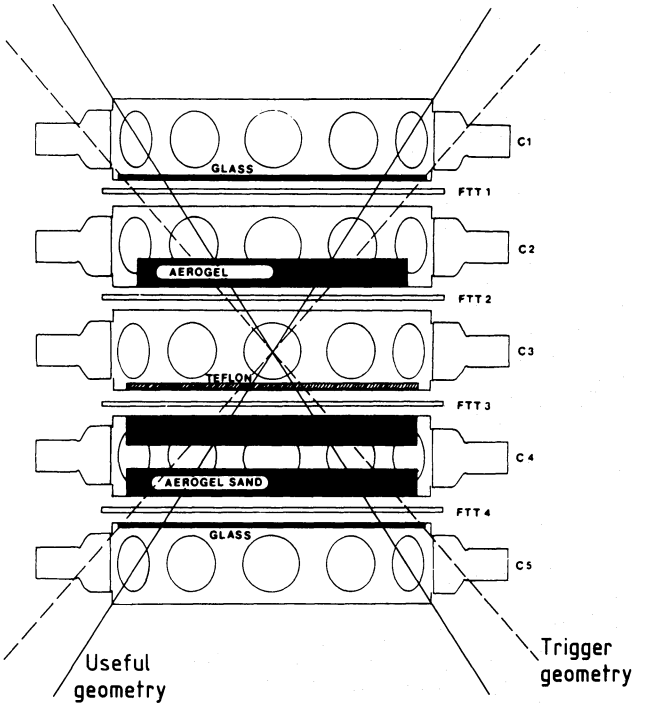

Fig. 1. Detector configuration. *C1-C5*: Cerenkov counters. *FTT1-FTT4*: Flash tube trays. The coincidence circuit is triggered by all particles going through the glass radiators of C1 and C5 ("triggered geometry"). Only particles going through the covers of counters C1 and C5 are selected for analysis ("useful geometry"). The maximum incidence angle for these particles is 31°5

2.2. Cerenkov counters

The determination of the charge and momentum of each incoming particle relies upon the double Cerenkov technique (Corydon-Petersen et al., 1970); the three inner detectors are used primarily for velocity determination and the top and bottom counters for charge determination. The main characteristics of the counters are summarized in Table 1.

Each counter is made of one or two discs of radiating material within a light diffusion box of 60 cm in diameter and viewed by twelve 5 inch photomultiplier tubes. Silica aerogel is used as a Cerenkov material in both C2 and C4 counters. This new material with adjustable refractive index was developed by Cantin et al. (1974), in order to match the particle spectrum observable along the HEAO-3 orbit. The C2 radiator is a mosaic of hexagonal blocks of 5.6 cm thick aerogel; its refractive index is 1.052. Silica aerogel is also used for the C4 counter, but with a lower refractive index (1.012). This material being too brittle to be used in the form of blocks was crushed up into an "aerogel sand", kept in place in the diffusion box by a mylar window. This sand is made of grains about 2 mm in diameter. Two such radiators, each 5.5 cm thick, are placed within the diffusion box (Cantin et al., 1981).

2.3. Flash tubes hodoscope

The hodoscope serves the dual purpose of allowing corrections for geometrical variations in the Cerenkov counter response and of determining the particle arrival direction in the geomagnetic field (Rotenberg et al., 1981; Lund et al., 1981a). In addition, it helps to select against nuclear interactions.

The hodoscope consists of 4 arrays of two perpendicular layers of flash tubes, allowing the determination of the coordinates of the particle impact point in each array plane. Each layer includes 128 glass tubes 670 mm long, with an outer diameter of 4.85 mm and a wall thickness of 0.2 mm. The tubes are filled with neon at atmospheric pressure, mixed with 0.2 torr of H_2 and 0.1 torr of O_2.

When a particle has triggered counters C1 and C5 with consistent signals in both counters, a high voltage pulse of 3 kV amplitude is applied across the tubes after a certain delay. The purpose of this delay, which is an increasing function of the signals in C1 and C5, is to suppress the flashes due to lightly ionizing knock on electrons, without degrading the efficiency for

Table 1

Counter	Radiator material	Refractive index	Momentum threshold (GeV/c/n)	Density ($g\,cm^{-3}$)	Thickness (cm)	Mean number of photoelectrons ($Z=1$, $\beta=1$)
C1, C5	F2 glass	1.64	0.72	3.61	1.0	40
C3	Teflon	1.33	1.065	2.18	1.5	30
C2	Aerogel block	1.052	2.844	0.26	5.6	15
C4	Aerogel sand	1.012	6.1	0.038	2×5.5	6

seeing the primary nucleus. Typically, the delay varies from 2.5 μs for Be nuclei to 11.5 μs for Ni nuclei. However, the layer efficiency for an incident particle is not 100% due to dead and "weak" tubes contained in the layer; furthermore it varies with the charge and the energy of the particle. To estimate this efficiency, we took advantage of the overdetermination of the straight lines in the hodoscope, which allows the determination of the efficiency of each layer independently. The global efficiency is then computed from these partial efficiencies (Rotenberg et al., 1981).

2.4. General characteristics of the instrument

The instrument weighs 350 kg, requires 35 watts of power and a data flow rate of 1.6 kbit/s. The useful geometry is 0.070 m^2 sr for each direction of propagation. The data used in this study have been registered between Oct. 17, 1979 and June 12, 1980. The first date corresponds to the setting in final configuration of the experiment, 25 days after launch of the HEAO-3 spacecraft. The last date is the day before the failure of the high voltage pulser of a flash tube array, resulting in a high loss of efficiency of the hodoscope. During that period of time, the drift of the counters has been less than 3%, so that drift corrections could be made accurately.

The number of "good" events registered (non interacting particles) is about 7 millions nuclei with charges between 4 and 28.

3. Data analysis procedure

3.1. Charge determination. Selection criteria

According to its energy, the charge of a particle is measured by 2, 3 or 4 counters, those which are nearly saturated in the relevant energy range (Table 1):

2 counters (2 glass counters) up to 2.4 GeV/n

3 counters (2 glass counters + teflon) from 2.4 to 6.4 GeV/n

4 counters (2 glass counters + teflon + aerogel block) above 6.4 GeV/n.

An additional counter with higher threshold measuring velocity (Teflon at low energy, aerogel block at medium energy and aerogel sand at high energy) is used to eliminate the residual velocity dependence from the signals of the lower threshold charge determining counters. By this way, we get for each particle 2, 3 or 4 charge estimates, depending on its energy. The adopted charge Z_w is a weighted linear combination of the charge estimates Z_i obtained from the different counters (the weight w_i being proportional to the inverse squared standard deviation of each counter). A final integer charge and a "charge quality" is assigned to each particle. This charge quality is a measure of the consistency in the charge assignment. The value adopted for this quantity is the following:

$$\delta Z = \sqrt{\sum w_i |Z_w - Z_i|^2}$$

where the sum is taken over the 2, 3 or 4 charge counters, according to the energy range considered.

When δZ exceeds an acceptable value, the particle is rejected for lack of consistency in the charge assignments. This condition helps to reject the particles interacting in the instrument, although most of them are already rejected by the trigger conditions and the additional requirement of a single straight line track per event in the hodoscope.

An example of the charge histogram obtained by this method is shown in Fig. 2. The charge resolution in the whole energy-charge domain is always better than 0.2 charge unit (the extrema being 0.12 for $Z=10$ in the aerogel block range and 0.20 for $Z=26$ in the teflon range) and the overlap between charges is insignificant. So, no overlap correction is needed, except, as will be discussed later, for Mn and Co.

In all studies reported in this paper, additional criteria are used to select the "good" events:

— The particles are required to go through the top cover of the two glass counters C1 and C5, in order to reject the particles hitting the photomultiplier tubes viewing the glass radiators (Fig. 1).

— In the elemental composition studies, we reject the particles having a momentum per nucleon P close to the momentum/n threshold corresponding to the rigidity cut off R_c ($\sim 2P$) calculated for the position and direction of the particle. Therefore the relative elemental abundances cannot be affected by the differences in mean mass between the various elements. In practice, we accept only particles with $P > 0.6\, R_c$.

3.2. Determination of the momentum/nucleon of the particle

The momentum of a particle of charge Z and incidence angle Θ is computed independently for the 3 velocity counters C2, C3 and C4. The observed signal value is first corrected for the incidence angle and the impact position of the particle in the counter. We apply a mapping correction derived from in-flight calibration with C and O nuclei, as described in Lund et al. (1981a). Then we determine the momentum of the particle by propagating it into the telescope and computing the expected signal from the counter considered: the momentum is incremented until the difference between the calculated and the observed signals is lower than 0.5%. In this computation, we consider three components contributing to the signal of a counter:

(i) The primary Cerenkov light, described by the classical expression:

$$Q = Z^2 Q_0 (1 - P_0^2/P^2) \quad (1)$$

where Q_0 is the maximum primary contribution for a particle of charge 1 and velocity equal to the velocity of light. P_0 is the

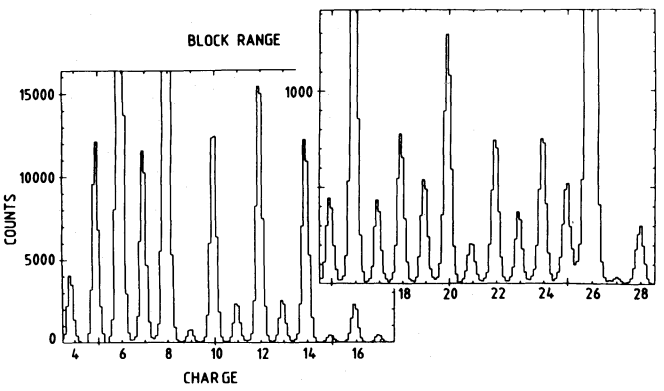

Fig. 2. Charge histogram in the aerogel block energy range (2.35 to 6.4 GeV/n), with 10 channels per charge unit

momentum/n threshold of the counter, P is the momentum/n of the particle.

(ii) The residual scintillation light, assumed to be energy independent and proportional to Z^2. This component, produced by the material lining the counter (millipore paper, mylar window) is estimated from the signals given by the particles below the Cerenkov threshold.

(iii) The Cerenkov light due to knock on electrons. This contribution, which is energy dependent, has been evaluated by Lund et al. (1981b).

The parameters of the formula for the primary Cerenkov contribution are determined as follows:

(i) The parameters P_0 for the teflon ($P_0 = 1065$ MeV/c) and for the aerogel block ($P_0 = 2844$ MeV/c) were derived from accelerator measurements with heavy ion beams at the Bevalac.

(ii) The parameter P_0 for the aerogel sand was derived from a study of the geomagnetic transmission function in the sand for various cut off values. A threshold of 6100 MeV/c was thus determined, in fair agreement with that derived from measurements of its refractive index (Engelmann and Cantin, 1978).

(iii) The parameters Q_0 for the teflon and the aerogel blocks are accurately determined since cuts in the sand spectrum can be used to select very high energy particles. Figure 3 shows the signal distribution of iron nuclei in teflon and block counters for momenta $P > 9$ GeV/c/n. In order to take into account the effect of the momentum spectrum, especially for the sand counter, we have made a Monte Carlo simulation of the observed peaks. Given a momentum spectrum at Earth, taken from a standard propagation program, two parameters were varied, namely the Q_0 and the fluctuation arising from photoelectron statistics and pathlength fluctuations in the detector. The adopted Q_0 values were then found by a χ^2 test. Figure 4 shows the observed signal distribution in the sand counter for the iron particles (solid line), together with the best fit distribution (dotted line). The method turns out to be fairly accurate since Q_0's were determined to $\sim 0.1\%$ for teflon and aerogel block and $\sim 0.5\%$ for aerogel sand. The Q_0 value derived for iron nuclei was used to assess the Q_0 for other nuclei, assuming the Z square dependence for the light output. This dependence was checked to be in excellent agreement with the data down to oxygen. For lower charges, a correction for non-linearities in the electronics was found necessary.

From Eq. (1), we can derive the uncertainty in momentum due to the uncertainty on Q_0:

$$\frac{dP}{P} = -\frac{(P/P_0)^2 - 1}{2} \cdot \frac{dQ_0}{Q_0}. \quad (2)$$

Practically, we use the teflon momentum up to 3 GeV/c, the block momentum up to 7.3 GeV/c and the sand momentum up to 18 GeV/c. Therefore P/P_0 is always less than 3, leading to a systematic error on P lower than 0.5% for teflon and aerogel block and 2% for aerogel sand. Note that, as discussed by Juliusson (1974), the maximum resolvable momentum P_{max}, which corresponds to a signal 1σ below the maximum signal Q_0 is given by:

$$\frac{P_{max}}{P_0} = Q_0^{0.25}.$$

This leads for the sand counter and Be nuclei to $P_{max}/P_0 = 3.5$ and to higher values of this ratio for $Z > 4$.

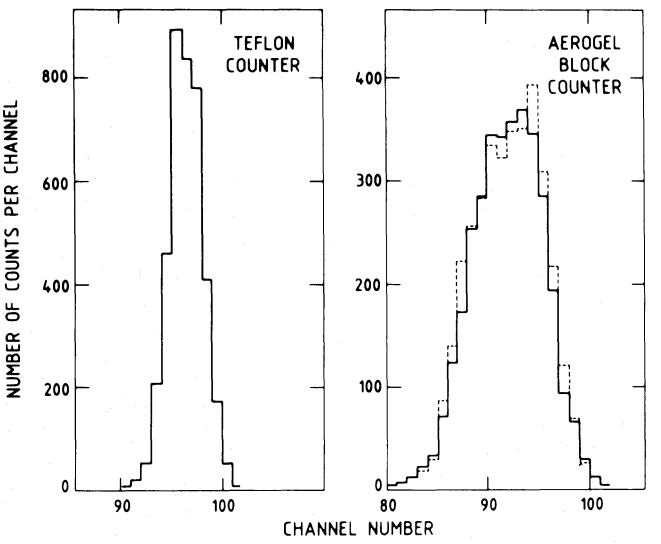

Fig. 3. *Solid line*: observed distribution of iron nuclei signals in teflon and block counters for momenta $P > 9$ GeV/c/n. *Dotted line*: best fit given by the Monte Carlo program

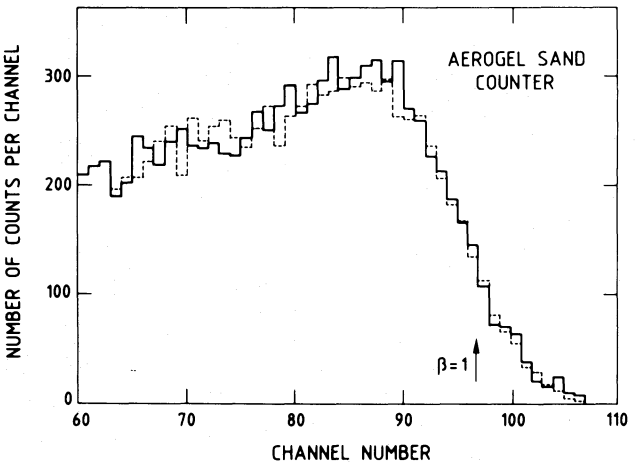

Fig. 4. *Solid line*: observed distribution of iron nuclei signals in sand counter. *Dotted line*: best fit. The arrow indicates the position of the maximum expected signal at $P = +\infty$

This momentum has been used for isotope analysis in the aerogel block range (Ferrando et al., 1988a). In this work, a transmission function combining momentum and cut off value computed with the help of a geomagnetic field model was derived. It was found that the momentum was consistent with the geomagnetic rigidity cut off within 2%. This provides an independent check of our momentum determination.

4. Derivation of the relative abundances of the elements

4.1. Energy dependence

In this part of the study, we do not need to get the true interplanetary spectrum of each element. We can work with the

observed spectrum, resulting from the folding of the interplanetary momentum spectrum with the percentage of time spent at different rigidity cut offs: the corresponding weighting factor is the same for all elements.

There is still the problem of connecting the momentum spectra measured by different counters with different resolutions. Here we follow the method presented in Engelmann et al. (1983): we use teflon spectra up to ~ 2.4 GeV/n, then aerogel block spectra from ~ 2.4 to 6.4 GeV/n, and sand spectra above ~ 6.4 GeV/n. These limits, defining the three energy ranges are chosen slightly higher than the threshold values mentioned in Table 1, as fluctuations in background signal prevent the use of a counter too close to its threshold.

In the high "sand energy" region, the signal is distorted by the signal broadening due to the finite resolution of the sand counter. To correct for this effect, we simulate how particles with a given energy are redistributed into measured signal bins, according to both the finite resolution of the counters and the spectral index, then we use these simulation results to correct the number of particles in a given energy window, as explained by Juliusson (1974).

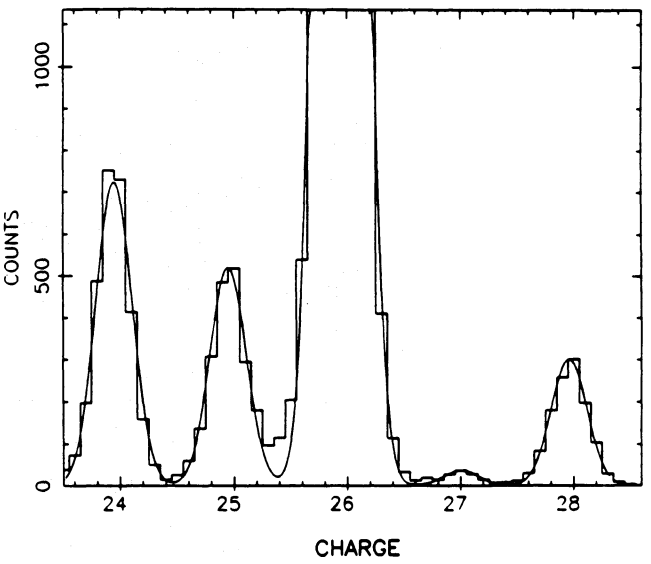

Fig. 5. Enlarged charge histogram and Gaussian best fit near the iron peak, in the aerogel block energy range

4.2. Groups of charge

Particles are grouped into two categories according to their charge: for charges $Z \geq 10$, the time of flight measurement is accurate enough to tell us unambiguously the direction of propagation in our double ended instrument. This is no more the case below $Z = 10$. These lighter nuclei are therefore accepted only when one of the directions is blocked by the Earth's shadow, where the geomagnetic field allows the particles to reach the instrument from one direction only. We also count the proportion of particles of $Z \geq 10$ in the Earth's shadow, in order to get the normalization factor between the two sets of data. The charge range covered in the present study extends from 4 to 28. The lower limit is imposed by the resolution of the counters, and the upper limit by the statistics due to the relatively small geometry resulting from the selection criteria used in the present study. However, by relaxing some selection criteria, it has been possible to use an extended acceptance geometry, in order to get enough statistics for the very rare elements above $Z = 28$. The results have been reported in Byrnak et al. (1983).

4.3. Corrections for charge selection, nuclear interactions and flash tube efficiency

With the consistency criteria used for the signals from the counters, the overlap between charges is insignificant and no correction for charge selection is needed, except for Mn and Co which are slightly contaminated by the far more abundant Fe nuclei. For this charge region, the charge histograms have been plotted for each energy window and fitted by a succession of Gaussian peaks (Fig. 5). A small excess is apparent on the left-hand side of the Fe peak. It can be attributed to the few events in which an Fe nucleus interacts just near the end of its trajectory through the last counter of the instrument: its apparent charge is then slightly lower than 26, but it can still pass the selection criteria. Those events, which represent only 0.3% of the iron peak are rejected by the fitting procedure.

On the average, particles traversing the instrument, go through 16 g/cm^2 of matter of mean atomic number $Z_t = 30$. Nearly all interacting particles are rejected (except for the few mentioned above) by requiring a single straight line for the track in the hodoscope and consistency in the charge assignment given by the counters (Sect. 3.1). In order to correct for the loss of particles due to these interactions, we have used Bradt and Peters type charge changing cross sections, giving the best fit to the total cross section measurements for $Z \geq 2$ (Westfall et al., 1979; Ferrando et al., 1988b):

$$\sigma = 57.3(A_p^{1/3} + A_t^{1/3} - 0.83)^2 \text{ mb}$$

A_p and A_t being the mass numbers of the particle and the target nuclei respectively.

The values of these nuclear interaction correction factors, taken to be energy independent, vary between 1.39 ± 0.02 for Be and 2.12 ± 0.08 for Ni. The quoted errors are mainly due to the total cross section errors, assumed to amount to 5%.

A last correction is applied to the data to account for the charge and energy dependence of the hodoscope efficiency. This efficiency is computed by selecting events with 3 or 4 points in each view and counting the proportion of these events detected by each layer. Compared to our previous work, a special care was taken to tail down all possible causes of systematic errors. In particular, we have evaluated the probability for a two points line event to the partly due to extra-flashes (flashes not directly due to the primary particle); this effect leads to an apparent increase of the hodoscope efficiency for low charges (2.5% for Be). Also the probability for a non interacting particle to give a 3 points line accompanied by another 3 points line due to random configuration of extra flashes was evaluated. If not taken into account, this effect tends to decrease the hodoscope efficiency for high charges (by $\sim 10\%$ for Fe nuclei at medium energy (3.5 GeV/n), and still more at higher energies). Taking this effect into account, we estimate that the Fe efficiency is known with an accuracy of 2% at 1 GeV/n, 3% at 3.5 GeV/n and 5% at 15 GeV/n.

The hodoscope efficiency at ~ 5 GeV/n is maximum around charge 14 (0.90 for Si ions), decreases only slightly at higher charges (0.88 for Fe ions), but appreciably towards lower charges

(0.86 for O and 0.76 for B ions). A slight energy dependence is observed, the efficiency being lower at higher energy (for C ions it is about 0.88 at 1 GeV/n and 0.77 at 20 GeV/n).

The correction factors used to correct for the loss of particles due to nuclear interactions and to the hodoscope efficiency have been plotted in Fig. 6, together with the combined correction factors. The latter correction factor is relatively large, varying between 1.82 ± 0.05 for oxygen nuclei and 2.42 ± 0.12 for Ni nuclei. However, when normalized to oxygen, the correction factor is at maximum equal to 1.35.

4.4. Relative abundances of elements of charge 4 to 28

These correction factors have been applied to the relative momentum spectra of all elements, derived from the signal histograms, as explained above (Sect. 4.1). The resulting abundance ratios at various energies are presented in Table 2, normalized to $O = 1000$. One σ statistical errors are given.

A systematic error on the combined correction factor (product of the nuclear interaction correction factor and of the efficiency correction factor) should also be taken into account. This error has been evaluated for 3 energy windows (1, 3.35 and 16.2 GeV/n) in Table 3. For widely different charges Z_1 and Z_2, a reasonable estimate of the error on the abundance ratio is the quadratic sum of the errors on both type of nuclei Z_1 and Z_2 (for example, the total error on the Fe/O ratio is $\sim 5.2\%$). For nearly adjacent charges, an upper limit of the systematic error is given by the difference between the systematic errors on each element (for example, the error on B/C is $\sim 0.4\%$).

The energy/nucleon limits corresponding to the 14 energy windows presented in Table 2 are the following:

— in the teflon range: 0.55, 0.70, 0.91, 1.11, 1.40, 1.82, 2.35 GeV/n;

— in the aerogel block range: 2.35, 2.96, 3.79, 4.89, 6.42 GeV/n;

— in the aerogel sand range: 6.42, 8.60, 12.0, 17.8 GeV/n.

The last window is an integral momentum window ($E > 17.8$ GeV/n). It is transformed into a differential window, as explained in Appendix 1. The first window can be safely defined only at low charges ($Z < 10$). At higher charges, the range of the particle becomes comparable to the telescope thickness, so that some particles of lower energy and/or larger incidence angle are absorbed in the telescope matter.

To illustrate the results obtained in this field, we have plotted the abundance ratios of some primary elements as a function of the energy, in Figs. 7 and 8.

There are slight differences between the results presented here and those previously reported by our group (Engelmann et al., 1981, 1983). As an example, we find now for the abundance ratio of B/C between 0.8 and 1.5 GeV/n values $\sim 2\%$ higher and between 2 and 5 GeV/n $\sim 4\%$ lower than our previous values. These differences can be mainly attributed to an improved efficiency correction C_e, as mentioned above, and to a more accurate interaction correction factor C_n, based on recent cross section data. For example, at medium energy (~ 5 GeV/n), C_e is now 3.5% lower for B, 1% lower for C and N, 2% lower for Si and Ca, unchanged for Fe. As regards C_n, it is now 0.5% higher for B and C, 1% lower for Si and 2.5% lower for Fe. These revised B/C values have some implications on the characteristics of the propagation derived from this ratio, and therefore on the source abundance of N, as will be discussed in Sect. 6.1. For comparatively rare elements, the same statistical fluctuations are observed in both studies, which is not surprising since they make use of nearly the same sample of particles. This is particularly visible on the Ni/Fe ratio, whose more or less erratic behaviour, probably due to the limited statistics and to the above mentioned systematic errors, looks like our previously reported results (Perron et al., 1981).

For clarity in the figures, we did not attempt at this stage to plot the data published by other experimenters. The interested reader is referred to the papers mentioned in Table 4, with the indication of the charge and energy ranges covered by each experiment.

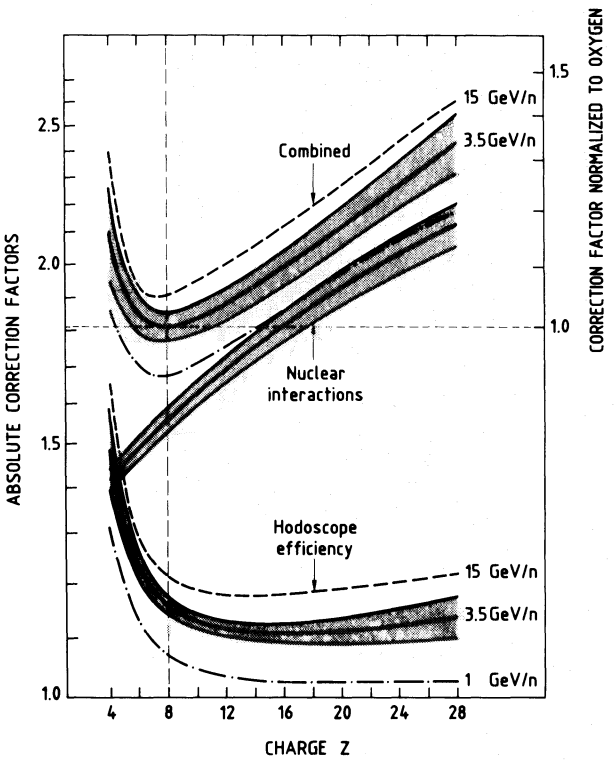

Fig. 6. Correction factors for hodoscope efficiency, for nuclear interactions and combined correction factor. *Solid line*: correction factors at 3.5 GeV/n. *Hatched area*: uncertainty on these coefficients of correction. *Dashed line*: correction factors at 15 GeV/n. *Dotted line*: correction factors at 1 GeV/n

5. Derivation of the absolute energy spectra

5.1. Methods applied

As mentioned in Sect. 4.1, for relative abundance measurements, we can directly use the observed momentum spectra of the elements (we had however to exclude particles of rigidity close to the geomagnetic cut off in order to avoid mass/charge dependent biases).

Now if we want to get the true spectrum of the particles, as they would be observed outside the magnetosphere, we have two possibilities:

Table 2. Relative abundances of heavy elements, normalized to O≡1000. Energies in GeV/n

Z	E= 0.62	0.80	1.00	1.25	1.60	2.10	2.65
4	85.8 ± 3.8	105.5 ± 3.4	108.4 ± 3.2	126.1 ± 2.9	118.6 ± 2.1	120.3 ± 2.1	120.2 ± 2.1
5	354.4 ± 7.3	362.3 ± 5.9	365.4 ± 5.7	364.9 ± 4.7	356.3 ± 3.6	321.0 ± 3.3	307.5 ± 3.2
6	1104.0 ±12.7	1108.7 ±10.2	1089.6 ± 9.6	1092.1 ± 8.0	1115.4 ± 6.2	1073.3 ± 5.8	1076.4 ± 5.9
7	313.0 ± 6.8	314.7 ± 5.4	319.4 ± 5.2	300.8 ± 4.2	302.9 ± 3.2	291.6 ± 3.0	283.6 ± 3.0
8	1000.0 ±12.0	1000.0 ± 9.6	1000.0 ± 9.2	1000.0 ± 7.6	1000.0 ± 5.8	1000.0 ± 5.6	1000.0 ± 5.6
9	27.1 ± 2.0	24.0 ± 1.5	22.0 ± 1.4	21.5 ± 1.0	20.9 ± 0.9	19.8 ± 0.8	20.7 ± 0.8
10	151.9 ± 3.5	162.0 ± 2.9	167.6 ± 2.8	157.6 ± 2.2	157.3 ± 1.7	152.2 ± 1.6	158.4 ± 1.6
11		34.7 ± 1.3	35.6 ± 1.3	34.7 ± 1.1	34.2 ± 0.8	33.0 ± 0.8	32.7 ± 0.8
12		208.7 ± 3.3	206.7 ± 3.1	206.5 ± 2.6	203.4 ± 2.0	198.4 ± 1.9	202.4 ± 1.9
13		35.7 ± 1.4	34.6 ± 1.3	36.4 ± 1.1	34.1 ± 0.8	35.1 ± 0.8	35.8 ± 0.8
14		152.6 ± 2.9	158.4 ± 2.8	155.4 ± 2.3	154.6 ± 1.7	151.7 ± 1.6	156.0 ± 1.7
15		7.2 ± 0.6	7.7 ± 0.6	7.1 ± 0.5	6.9 ± 0.4	6.8 ± 0.4	6.9 ± 0.4
16		30.9 ± 1.3	34.6 ± 1.3	30.9 ± 1.0	31.0 ± 0.8	29.5 ± 0.7	31.8 ± 0.8
17		6.4 ± 0.6	7.5 ± 0.6	7.2 ± 0.5	7.4 ± 0.4	6.9 ± 0.4	6.5 ± 0.4
18		13.1 ± 0.9	14.8 ± 0.9	14.0 ± 0.7	13.2 ± 0.5	13.1 ± 0.5	13.5 ± 0.5
19		9.8 ± 0.8	11.3 ± 0.8	9.4 ± 0.6	9.8 ± 0.5	8.8 ± 0.4	8.9 ± 0.4
20		22.0 ± 1.1	23.4 ± 1.1	23.4 ± 0.9	22.3 ± 0.7	19.8 ± 0.6	22.3 ± 0.7
21		4.7 ± 0.5	5.4 ± 0.5	5.4 ± 0.4	5.0 ± 0.3	3.8 ± 0.3	4.0 ± 0.3
22		14.3 ± 0.9	16.4 ± 1.0	15.0 ± 0.8	14.6 ± 0.6	13.8 ± 0.5	13.6 ± 0.5
23		6.4 ± 0.6	7.0 ± 0.6	7.0 ± 0.5	7.7 ± 0.4	7.2 ± 0.4	6.9 ± 0.4
24		13.6 ± 0.9	15.7 ± 0.9	16.3 ± 0.8	14.0 ± 0.6	13.6 ± 0.5	15.4 ± 0.6
25		6.9 ± 0.6	8.4 ± 0.7	10.1 ± 0.6	9.0 ± 0.4	9.9 ± 0.5	9.5 ± 0.4
26		86.7 ± 2.4	95.1 ± 2.4	101.3 ± 2.0	101.2 ± 1.5	97.0 ± 1.5	105.7 ± 1.5
27		0.35 ±0.10	0.57 ±0.17	0.58 ±0.11	0.48 ±0.06	0.66 ±0.10	0.57 ±0.10
28		3.5 ± 0.5	4.1 ± 0.5	4.9 ± 0.4	4.7 ± 0.3	4.7 ± 0.3	5.6 ± 0.3

Z	3.35	4.30	5.60	7.50	10.60	16.20	35.00
4	121.2 ± 2.1	111.4 ± 2.0	107.2 ± 2.0	103.9 ± 1.8	87.3 ± 1.8	73.2 ± 2.1	
5	294.8 ± 3.0	264.1 ± 2.8	251.7 ± 2.8	225.4 ± 2.6	192.5 ± 2.5	162.0 ± 3.0	116.0 ± 2.2
6	1084.7 ± 5.7	1039.8 ± 5.4	1049.0 ± 5.5	1037.4 ± 5.4	986.3 ± 5.6	957.8 ± 7.1	958.5 ± 7.4
7	273.5 ± 2.9	269.4 ± 2.8	252.3 ± 2.7	234.8 ± 2.6	218.7 ± 2.6	201.5 ± 3.2	173.9 ± 3.1
8	1000.0 ± 5.4	1000.0 ± 5.3	1000.0 ± 5.3	1000.0 ± 5.3	1000.0 ± 5.6	1000.0 ± 7.0	1000.0 ± 7.8
9	19.0 ± 0.8	19.2 ± 0.7	18.1 ± 0.7	15.4 ± 0.7	15.5 ± 0.7	13.5 ± 0.8	10.1 ± 0.8
10	154.1 ± 1.5	155.8 ± 1.5	154.0 ± 1.5	154.5 ± 1.5	152.2 ± 1.5	153.9 ± 1.9	144.2 ± 2.1
11	28.5 ± 0.7	30.8 ± 0.7	29.9 ± 0.6	27.8 ± 0.6	26.1 ± 0.6	23.1 ± 0.7	19.3 ± 0.8
12	194.9 ± 1.7	202.9 ± 1.8	204.8 ± 1.7	192.0 ± 1.6	197.3 ± 1.8	199.6 ± 2.2	190.5 ± 2.5
13	33.8 ± 0.7	33.8 ± 0.7	33.2 ± 0.7	31.2 ± 0.7	31.3 ± 0.7	30.8 ± 0.9	30.0 ± 1.0
14	158.5 ± 1.6	160.3 ± 1.6	162.9 ± 1.5	161.2 ± 1.5	163.4 ± 1.6	175.3 ± 2.1	175.7 ± 2.4
15	6.5 ± 0.3	5.9 ± 0.3	6.2 ± 0.3	6.1 ± 0.3	5.3 ± 0.3	5.3 ± 0.4	4.7 ± 0.4
16	31.6 ± 0.7	30.1 ± 0.7	31.3 ± 0.7	31.0 ± 0.7	29.9 ± 0.7	31.2 ± 0.9	31.7 ± 1.0
17	6.4 ± 0.3	6.1 ± 0.3	5.8 ± 0.3	5.6 ± 0.3	5.2 ± 0.3	5.0 ± 0.4	3.9 ± 0.3
18	11.3 ± 0.4	11.0 ± 0.4	10.9 ± 0.4	10.0 ± 0.4	9.3 ± 0.4	9.7 ± 0.5	9.0 ± 0.5
19	7.6 ± 0.4	8.2 ± 0.4	8.4 ± 0.4	7.5 ± 0.3	6.1 ± 0.3	6.6 ± 0.4	5.4 ± 0.4
20	19.6 ± 0.6	19.4 ± 0.6	19.2 ± 0.6	18.4 ± 0.5	18.1 ± 0.6	18.2 ± 0.7	18.7 ± 0.8
21	4.1 ± 0.3	3.7 ± 0.3	3.4 ± 0.2	3.3 ± 0.2	3.1 ± 0.2	2.8 ± 0.3	2.9 ± 0.3
22	13.0 ± 0.5	11.9 ± 0.5	12.0 ± 0.4	10.3 ± 0.4	10.0 ± 0.4	10.0 ± 0.5	8.5 ± 0.5
23	5.8 ± 0.3	6.7 ± 0.3	5.6 ± 0.3	5.6 ± 0.3	5.2 ± 0.3	5.3 ± 0.4	4.3 ± 0.4
24	12.4 ± 0.5	13.9 ± 0.5	12.8 ± 0.5	12.1 ± 0.5	10.7 ± 0.4	11.8 ± 0.6	11.0 ± 0.6
25	9.7 ± 0.4	8.7 ± 0.4	9.3 ± 0.4	9.0 ± 0.4	8.8 ± 0.4	9.0 ± 0.5	9.3 ± 0.6
26	105.1 ± 1.4	108.9 ± 1.4	112.6 ± 1.4	107.2 ± 1.4	110.0 ± 1.5	125.6 ± 1.9	135.5 ± 2.3
27	0.37 ±0.07	0.60 ±0.10	0.75 ±0.10	0.58 ±0.09	0.38 ±0.06	0.61 ±0.12	0.52 ±0.11
28	5.9 ± 0.3	6.1 ± 0.3	5.7 ± 0.3	5.6 ± 0.3	7.0 ± 0.4	6.9 ± 0.4	6.7 ± 0.5

(i) either to use all particles above the geomagnetic cut off at the point of measurement (here again we must exclude particles of rigidity close to the cut off). In that case, we get a distorted spectrum, which can be corrected by applying an energy dependent correction factor, for the proportion of time spent at various rigidity cut offs during flight.

(ii) or to select only the particles registered at rigidity cut offs below that corresponding to the velocity threshold of the counter considered (as an example below 2.3 GV for the teflon counter). In this last approach, only a small proportion of particles are selected (about 10% in the case of the teflon counter), and therefore we cannot use directly this method to get the energy spectrum of a rare element like P or Cl. We can use it however to get the spectrum of a reference element like oxygen and derive the spectra of other nuclei by using their relative abundances with respect to the reference element, as given in Table 2. In that case of course, the accuracy of every point in each spectrum is limited by the statistical accuracy of the corresponding point of the oxygen spectrum.

The first method was used in our previous analysis (Juliusson et al., 1983). Practically, the spectrum corrected from the distorting effects of the geomagnetic cut off was obtained by an iteration process, using the observed momentum distribution of the particles and the rigidity cut off distribution. However, even if the process is converging, we cannot exclude the possibility of a residual bias. This is the reason why, in the present paper, we preferred to use a modified version of the second method: by a proper selection of data, we are able to determine absolute flux

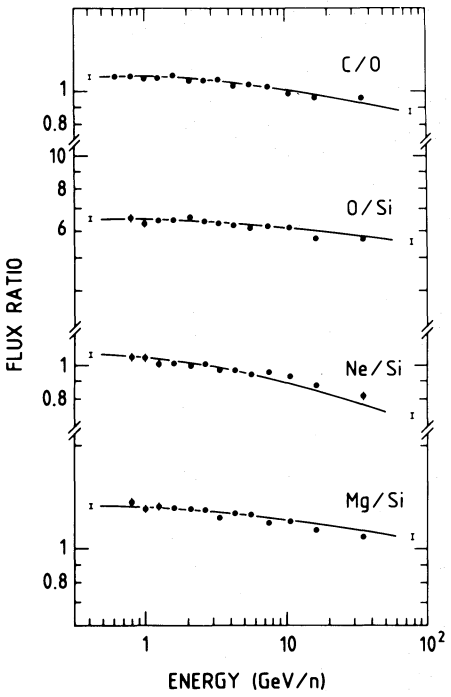

Fig. 7

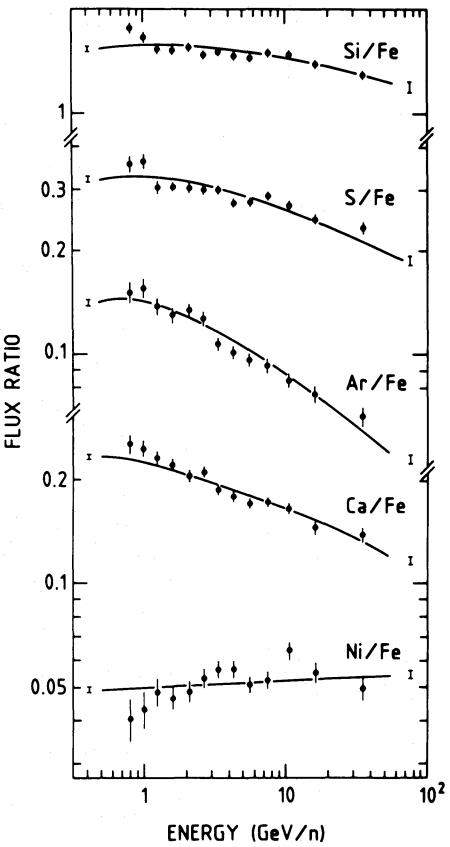

Fig. 8

Figs. 7 and 8. Observed and calculated abundance ratio of a few primary/primary elements. *Full curve*: ratio calculated in the leaky box model, with λ_{esc} as in Fig. 14. One σ statistical errors are given, which are often smaller than the representative point. The error bars plotted on both sides of each abundance ratio represent an estimate of the systematic error arising from the uncertainty on the value of the correction factor

values for each type of nucleus, in units of particles $m^{-2} sr^{-1} s^{-1} (GeV/n)^{-1}$. More precisely, to determine the spectrum above a threshold rigidity R_0, we have selected the data in such a way that:

(i) the geometry of the instrument is accurately known,

(ii) the geomagnetic cut off corresponding to all viewing directions of the telescope is lower than R_0,

(iii) the time during which these conditions are met is accurately measured.

All these conditions are fulfilled by selecting data when the telescope axis lies near the local vertical and when the vertical rigidity cut off is lower than $0.8\ R_0$. The instrument is then single-ended, since it is protected by the solid earth from particles propagating in the reverse direction. The acceptance geometry is known and we have verified that condition (ii) is fulfilled.

Practically, we first select periods of time when the angle between the telescope axis and the local vertical is lower than 25°. In order to have a well defined restricted geometry, we require in addition that the impact points of the particle in the top and bottom counters lie within a circle of 52 cm in diameter, i.e. well inside the radiators of the charge counters, which are 60 cm in diameter. In these conditions, the maximum acceptance angle of the telescope is 28° and the geometrical factor: $F = 413\ cm^2\ sr$. We then derive the oxygen spectrum between 0.55 and 2.4 GeV/n from data registered at rigidity cut off values smaller than 1.85 GV and that above 2.4 GeV/n from data registered at cut off values smaller than 5.0 GV, so as to improve statistics.

The absolute differential flux ϕ of a certain type of nucleus at an energy E is given by:

$$\phi = NC_n C_e / T\Delta EF$$

where N is the number of nuclei counted in the energy window of width ΔE during the time T cumulated over all selected periods of time. C_n and C_e are the correction factors for nuclear interactions and hodoscope efficiency, already mentioned in Sect. 4.3.

5.2. *Solar modulation and periods of time selected*

During the period of time when good data have been collected (from Oct. 17, 1979 to June 12, 1980), several large Forbush decreases occurred, associated with periods of high magnetic activity (Fig. 9). By applying the same selection criteria as was done for the absolute spectra, we could calculate the daily average flux of ions of charge $Z \geq 6$ and energy $E > 0.8$ GeV/n. This flux J has been plotted as a function of the daily index D of the Deep River neutron monitor (Fig. 10). The statistical error on each flux value is 5%. The correlation between J and D is found to be:

$$J = 2.54\ 10^{-3} D - 8.83$$

with a linear correlation coefficient of 0.585.

The lowest values observed for the flux J are in good correlation with periods of Forbush decrease. The deformation of the shape of the energy spectrum caused by these interplanetary

perturbations is not calculable since the rigidity dependence of this type of modulation is highly variable from event to event (Fenton et al., 1983). This is the reason why, for the determination of the absolute spectra, we decided to exclude these periods from the analysis. Practically, we processed the 14 magnetic tapes registered during relatively quiet periods and discarded the 6 tapes corresponding to periods of Forbush decrease and high magnetic activity (dashed area in Fig. 9).

Table 3. Evaluation of the systematic errors on the combined correction factor (nuclear interactions + hodoscope efficiency) for 3 energy windows. (In brackets, statistical errors). The errors are given in %

Z \ E(GeV/n)	1.0	3.35	16.2
4	6.2 (3.0)	7.2 (1.7)	8.1 (2.9)
5	2.7 (1.6)	3.2 (1.0)	4.0 (1.8)
6	2.5 (0.9)	2.9 (0.5)	3.6 (0.7)
7	2.3 (1.6)	2.5 (1.0)	3.2 (1.6)
8	2.1 (0.9)	2.2 (0.5)	2.8 (0.7)
9	2.2 (6.3)	2.3 (4.2)	2.7 (5.9)
10	2.2 (1.7)	2.3 (1.0)	2.7 (1.2)
11	2.3 (3.6)	2.3 (2.5)	2.8 (3.0)
12	2.3 (1.5)	2.3 (0.9)	2.8 (1.1)
13	2.4 (3.8)	2.4 (2.1)	2.9 (2.9)
14	2.4 (1.8)	2.5 (1.0)	2.9 (1.2)
15	2.5 (7.8)	2.6 (4.6)	3.0 (7.5)
16	2.6 (3.8)	2.7 (2.2)	3.2 (2.9)
17	2.7 (8.0)	2.8 (4.7)	3.3 (8.0)
18	2.9 (6.1)	3.0 (3.5)	3.5 (5.1)
19	3.0 (7.0)	3.2 (5.3)	3.7 (6.0)
20	3.2 (4.7)	3.5 (3.0)	3.9 (3.8)
21	3.4 (9.2)	3.6 (7.3)	4.1 (10.7)
22	3.5 (6.1)	3.8 (3.8)	4.3 (5.0)
23	3.6 (8.6)	4.0 (5.2)	4.7 (7.5)
24	3.7 (5.7)	4.1 (4.0)	5.1 (5.0)
25	3.9 (8.3)	4.3 (4.1)	5.5 (5.5)
26	4.0 (2.5)	4.5 (1.3)	6.0 (1.5)
27	4.1 (30.)	4.7 (19.)	6.8 (20.)
28	4.2 (12.)	4.8 (5.0)	7.9 (5.8)

5.3. *Results*

In Table 5, two values of the oxygen flux are given for each energy window:

(i) absolute values: ϕ in units of $m^{-2}\,sr^{-1}\,s^{-1}\,(GeV/n)^{-1}$;

(ii) "flattened values": $\phi \times E^{2.5}$ in units of $m^{-2}\,sr^{-1}\,s^{-1}\,(GeV)^{1.5}$.

The standard error is also given with each flux value. This error includes the statistical error and, in the case of the last two energy channels, the systematic error in the determination of the pulse height in the sand counter corresponding to $\beta = 1$ (Q_0; cf Sect. 3.2).

The corresponding flattened O spectrum has been plotted in Fig. 11. The flux is no longer normalized to the average of other published values at 10 GeV/n, as was done in Engelmann et al. (1985), but its value at this energy is still in good agreement with this average. The slope of the spectrum above 10 GeV/n is also in good agreement with that we have published earlier, but below that energy, we now find a slightly flatter spectrum. The cut off corrections, including penumbra effects had been probably underestimated in our previous analysis. No such corrections have to be applied presently since the data have been severely selected to prevent any bias by the geomagnetic cut off, at the expense of the statistics.

In comparison with other published data, HEAO-3 data above 10 GeV/n are on the lower side of the distribution, but the spread of the points is relatively large. At lower energies, the solar modulation is, as expected, stronger for HEAO-3 and Webber 81 than for all other experiments which were flown near solar minimum. The Mount Washington neutron monitor rates corresponding to the different experiments were 2365, 2190 and 2118 for Webber 77, HEAO-3 and Webber 81 respectively.

The spectrum of any element between $Z = 4$ and $Z = 28$ can be obtained by multiplying the oxygen flux values of Table 5 by the corresponding abundance ratios given in Table 2. The relative errors on these two numbers shall be quadratically summed to

Table 4

Year of data collection	Charge range	Energy range (GeV/n)	Reference
1970	$3 < Z < 28$	0.1–2	Webber et al., 1972
1972	$3 < Z < 28$	>20	Juliusson, 1974
1972	$3 < Z < 28$	2–150	Orth et al., 1978
1974	$5 < Z < 28$	>5	Caldwell, 1977
1975	$2 < Z < 28$	0.07–0.28	Garcia Munoz et al., 1979
1975	26 and 28	1–10	Minagawa, 1981
1975	$5 < Z < 28$	1.2–2.4	Dwyer and Meyer, 1985
1975	$5 < Z < 28$	1–10	Dwyer and Meyer, 1987
1976	$3 < Z < 28$	0.3–50	Lezniak and Webber, 1978
1976	$5 < Z < 26$	2–100	Simon et al., 1980
1977	$10 < Z < 28$	0.4–3	Young et al., 1981
1977	$2 < Z < 28$	0.6–1	Webber, 1982
1977	$16 < Z < 28$	0.3–1.2	Crane et al., 1983

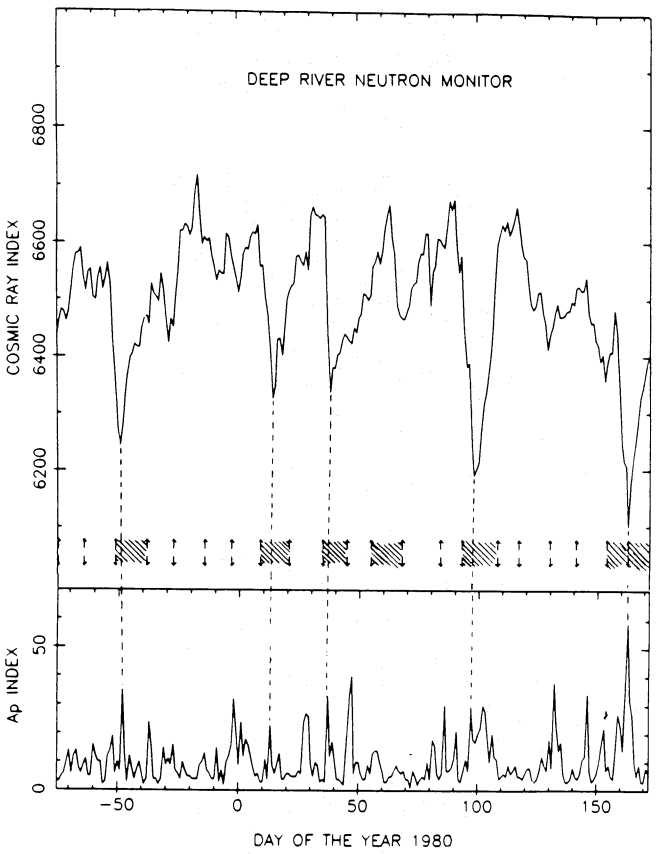

Fig. 9. *Top*: time profile of the daily index of the Deep River neutron monitor (average counts per hour/300). *Bottom*: A_p geomagnetic index (which is a linear daily index derived from the k_p indices). Each interval between two double arrows corresponds to the time interval covered by a magnetic tape of our data. The dashed areas correspond to the magnetic tapes rejected from the spectrum analysis

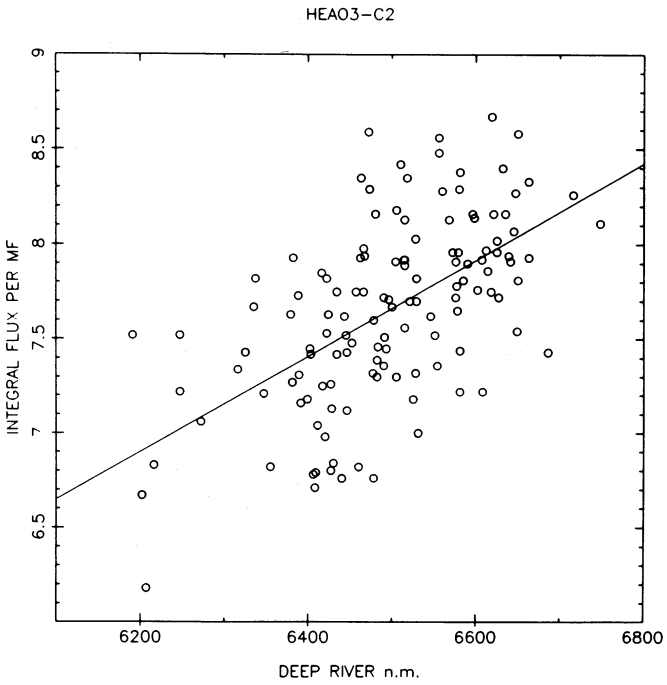

Fig. 10. Correlation between the HEAO3-C2 average daily flux of nuclei with charge ≥ 6 and energy >0.8 GeV/n and the Deep River neutron monitor index. The nuclei flux is given in counts per major frame (41 s). The statistical error on each point is $\sim 5\%$. The straight line corresponds to the linear correlation between the nuclei flux and the neutron monitor index

get the error on the flux derived by this way. As an example, this has been done for the Fe spectrum in Fig. 12. We see again the effect of solar modulation, which was stronger during the HEAO-3 flight than during all other measurements plotted in the figure.

6. Elemental abundances and energy spectra of cosmic rays at the source

6.1. The propagation calculation

For propagating cosmic rays back to their source, it is customary to perform a leaky box calculation. This has been widely used for presenting and interpreting the abundance ratio of cosmic ray nuclei (e.g. Garcia Munoz et al., 1987; Engelmann et al., 1985; Ormes and Protheroe, 1983). The leaky box calculation presented here makes use of the latest partial cross sections in hydrogen both calculated and measured by the New Hampshire group (Gupta and Webber, 1988, and references therein) and those in the interstellar helium (10% of hydrogen by number) measured by Ferrando et al. (1988b). It also takes care of ionization losses in neutral hydrogen and helium. Radioactive beta decays of long lived species in a medium with 0.3 hydrogen atom cm^{-3} are taken into account. The input source spectra are taken identical for all species, with a power law dependence in momentum. The modulation parameter characterizing the conditions prevailing in the interstellar medium in 1980 is taken equal to 600 MV (Lockwood and Webber, 1979, 1981). The nominal source abundance values assumed independent of energy have been adjusted from the data; they are given in Table 6. For rarer elements, we have assumed for the calculation

Table 5. Oxygen energy spectrum

E (GeV/n)	Flux ϕ $(m^{-2}s^{-1}sr^{-1}(GeV/n)^{-1})$	$\phi \times E^{2.5}$ $(m^{-2}s^{-1}sr^{-1}(GeV/n)^{1.5})$
0.62	2.695 ±0.042	0.82±0.01
0.80	2.205 ±0.035	1.26±0.02
1.00	1.675 ±0.030	1.67±0.03
1.25	1.504 ±0.025	2.63±0.04
1.60	1.091 ±0.018	3.53±0.06
2.10	0.753 ±0.013	4.81±0.08
2.65	0.496 ±0.006	5.67±0.07
3.35	0.335 ±0.004	6.90±0.09
4.30	0.220 ±0.003	8.41±0.11
5.60	0.132 ±0.002	9.80±0.14
7.50	0.073 ±0.002	11.25±0.18
10.60	0.0329±0.0006	12.05±0.22
16.20	0.0106±0.0004	11.15±0.45
35.00	0.0013±0.0002	9.17±1.25

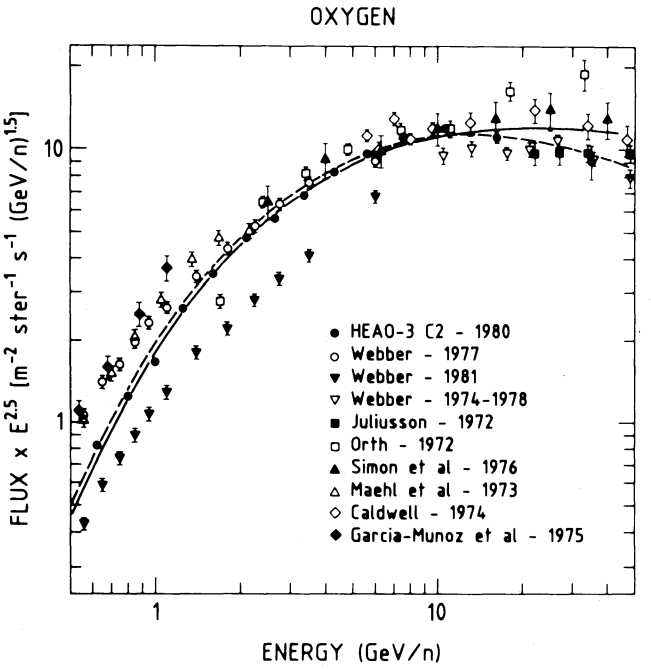

Fig. 11. "Flattened" oxygen spectrum obtained by multiplying the differential flux values (in particles $m^{-2}\,s^{-1}\,sr^{-1}\,(GeV/n)^{-1}$) by $E^{2.5}$, where E is the kinetic energy per nucleon of the particle. The year of data collection is given in the figure for each experiment. Observations are from Chappel and Webber 1981, Webber et al., 1985, Juliusson, 1974, Orth et al., 1978, Simon et al., 1980, Maehl et al., 1977, Caldwell, 1977, Garcia Munoz et al., 1977. *Full curve*: propagated spectrum for a kinetic energy source spectrum shaped as a power law in momentum, with a spectral index of 2.23 and a modulation parameter of 600 MV. *Dashed curve*: propagated spectrum for a kinetic energy source spectrum shaped as a power law in total energy, with a spectral index of 2.40, and a modulation parameter of 500 MV

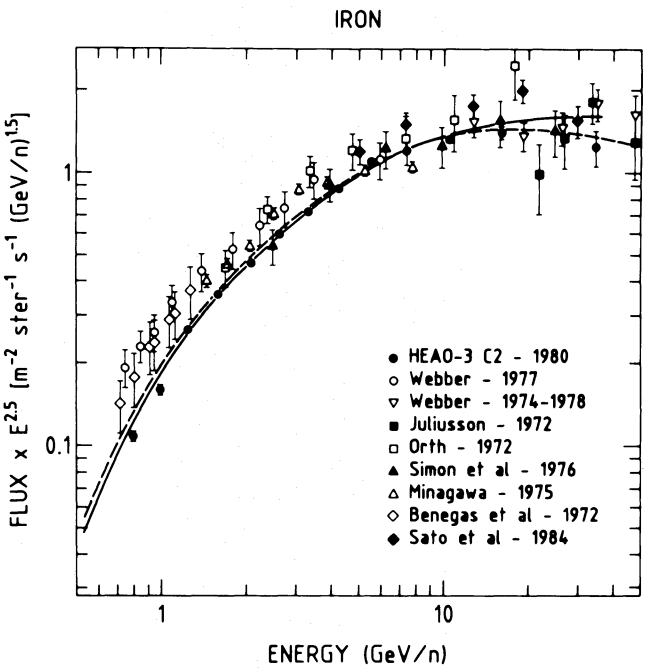

Fig. 12. "Flattened" iron spectrum. Same as in Fig. 11. Observations are from Chappel and Webber, 1981, Webber et al., 1985, Juliusson, 1974, Orth et al., 1978, Simon et al., 1980, Minagawa, 1981, Benegas et al., 1975, Sato et al., 1985

a local galactic abundance value with first ionization potential filtering (Meyer, 1985b).

By comparing the calculated and observed boron to carbon ratio, the following value of the escape length is obtained (Figs. 13 and 14):

$$\lambda_{esc} = 34.1\,\beta R^{-0.60}\,g\,cm^{-2} \quad \text{for } R > 4.4\,GV$$

$$\lambda_{esc} = 14.0\,\beta\,g\,cm^{-2} \quad \text{for } R < 4.4\,GV$$

where R and β are the interstellar values of the rigidity and the ratio of the velocity of the particle to the velocity of light. The good agreement observed for the boron-to-carbon ratio (Fig. 13) is also observed for other ratios at intermediate charges (Fig. 15).

In order to derive the source abundances of the most abundant elements, it is necessary to estimate the validity of the leaky box calculation throughout the energy and charge range covered by the HEAO-3 data. This is done by comparing the observed and calculated iron secondaries to iron ratio (Fig. 16). It is seen that the agreement is good at energies above ~ 5 GeV/n and becomes poorer below that energy. The calculation makes use of a set of cross sections obtained from accelerator measurements below ~ 2 GeV/n of unprecedented extent. Above this energy, the cross section values in hydrogen result from an extrapolation according to the empirical formula provided to us by Webber (Webber, 1987 and 1989). The cross sections in helium are

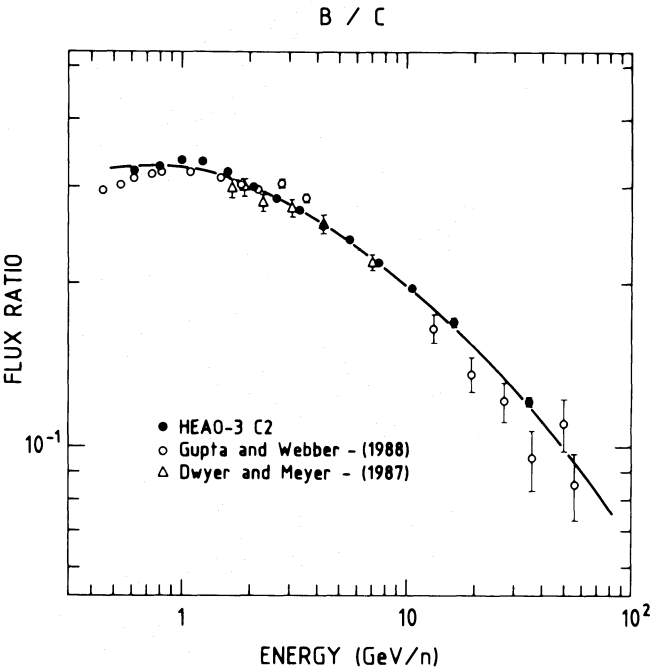

Fig. 13. Predicted and observed B/C ratio (see Fig. 7 caption)

calculated with the formula of Ferrando et al. (1988b). The good agreement above ~ 5 GeV/n makes it reasonable to assume that the apparent discrepancy at low energies is not entirely due to errors on the low energy cross section values. Several recent works have reported a similar conclusion, making the case for

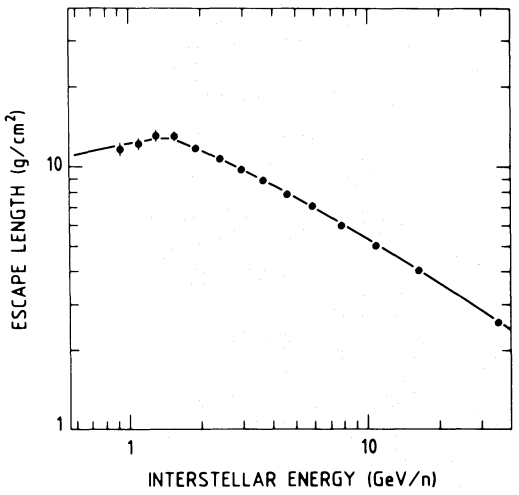

Fig. 14. Energy dependence of the escape length. *Solid circles*: escape length derived from the B/C ratio. *Continuous curve*: fit given by the law:

$\lambda_{esc} = 34.1 \beta R^{-0.60}$ g cm^{-2} for $R > 4.4$ GV

$\lambda_{esc} = 14.0 \beta$ g cm^{-2} for $R < 4.4$ GV

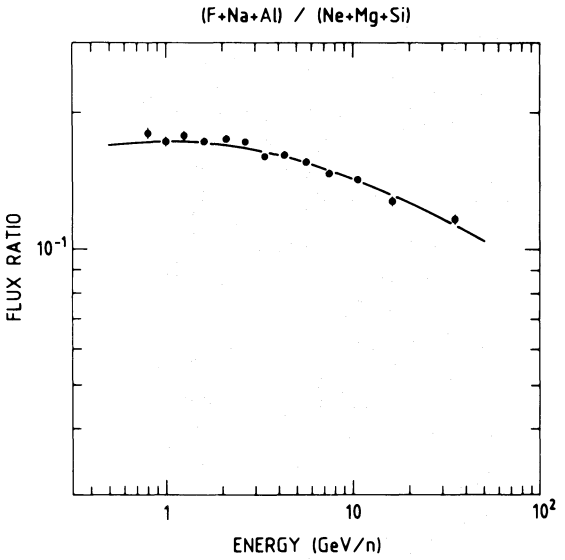

Fig. 15. Predicted and observed (F + Na + Al)/(Ne + Mg + Si) ratio (see Fig. 7 caption)

truncation of short path lengths at low energies (Garcia Munoz et al., 1987; Ormes and Protheroe, 1983; Soutoul and Ferrando, 1989). Note that this low energy discrepancy, which is increased by the incorporation of interstellar helium into our calculation, is still significant if the helium contribution is neglected: the propagation calculation repeated in pure hydrogen shows that for an equally good agreement with the boron to carbon ratio, the agreement at low energies seems still poorer than above 5 GeV/n (Fig. 16). Although a full discussion of the importance of cross section uncertainties and of the composition of the interstellar medium is beyond the scope of this paper (see Soutoul et al., 1990), we note that at energies above 5 GeV/n, the source abundances in the iron range can be reliably obtained from the leaky box calculation.

6.2. *Source abundances*

At each energy, the source abundances are adjusted in order to reproduce the observed abundances. Within the uncertainties no significant energy dependence is found (see Figs. 7 and 8). We adopt as cosmic ray source abundances the values averaged over the entire energy range, except for Ca, Ar, Fe and Ni, for which the average is taken only above 5 GeV/n, where the exponential distribution of pathlengths agrees better with the data (Sect. 6.1).

The derived source abundances are quoted in the Table 6, normalized to Silicon, together with three independent uncertainties arising from the uncertainty of the data themselves, and from propagation errors separated into cross sections and escape length uncertainties. Only elements for which a finite GCRS value (including errors) was found are listed in Table 6. The errors were estimated as follows.

The data uncertainty was computed from the scattering of the source abundances at each energy around their average value, in order to take into account possible systematic effects which could result in an error larger than that given by the simple statistics of the number of events. This procedure is justified since no energy dependence is visible in our data. The resulting uncertainty was always larger than the simple statistical uncertainty by a factor 1 to 3, except for P, K, and Ca, for which we adopted the statistical uncertainty.

The propagation uncertainties, which are systematic, were estimated at the energy of 5.6 GeV/n, with the following assumptions:

— For uncertainties arising from the production cross sections uncertainties for each element, 5% of accuracy for measured cross sections and 10% for unmeasured cross sections were assumed. Conservatively, they were added linearly. This uncertainty must be added quadratically to the data uncertainty, as it appears in Table 6.

— With the same assumptions on the cross sections for boron production, the uncertainty on the escape length necessary to fit the B/C ratio was estimated to be 11% at 5.6 GeV/n. It must be noted that, when comparing two elements, this "escape length uncertainty" results in a *systematic* error in the source abundances. For example, the C and O source abundances have an "escape length uncertainty" of 6.9 and 5.4% respectively, but the C/O source ratio has an "escape length uncertainty" of only 1.5%.

When the source abundances presented in Table 6 are compared with our previous results (Koch-Miramond, 1983; Engelmann, 1984; Lund, 1984), we find that the new values are quite compatible with the old ones within quoted errors for C, O, Ne, Mg, Si, Ca, Fe and Ni, but are lower by factors of 0.6 to 0.8 for N, Na, Al, Ar, Co.

These differences cannot be attributed to differences in the observed abundances since the present values (Table 2) do not differ by such a large factor from our previous values (Engelmann et al., 1983); they are mainly ascribed to differences in the production cross sections: the most sensitive elements to variations in cross section data are precisely the mainly secondary elements like N, Na, Al, Ar and Co. (At 5 GeV/n the fractions of surviving primary nuclei of these elements are 20, 17, 34, 30 and 46% respectively). As an example, if the production cross sections

Table 6

Element	GCRS	Statist. error (%)	Cross sec. error (%)	Combined error (%)	Systematic error on λ_{esc} (%)
C	424.9	0.74	1.49	1.66	6.9
N	25.4	3.12	24.8	25.0	28.8
O	526.3	0.50	0.49	0.70	5.4
Ne	58.0	1.85	4.65	5.0	7.6
Na	3.23	4.61	29.8	30.1	24.3
Mg	103.8	0.77	2.23	2.36	5.5
Al	7.78	3.31	19.7	16.0	14.3
Si	100.0	0.36	1.25	1.30	4.6
P	0.77	5.11	37.3	38.7	24.0
S	13.1	2.08	6.4	6.73	6.7
Ar	2.23	7.19	24.7	25.7	16.7
K	0.40	24.9	71.6	80.2	35.1
Ca	6.01	3.63	14.1	14.6	9.7
Fe	100.8	1.18	0.25	1.21	3.1
Co	0.19	29.2	12.6	31.8	8.5
Ni	5.68	3.49	0.21	3.5	2.9

Table 7

Element	GCRS	LG	GCRS/LG
C	424.9 ± 12.1	1023 ± 99	0.415 ± 0.042
N	25.4 ± 8.8	316 ± 31	0.080 ± 0.029
O	526.3 ± 5.6	2399 ± 201	0.219 ± 0.019
Ne	58.0 ± 3.4	347 ± 90	0.167 ± 0.044
Na	3.23 ± 1.26	5.9 ± 0.3	0.547 ± 0.199
Mg	103.8 ± 2.6	107 ± 5	0.970 ± 0.051
Al	7.78 ± 1.46	8.5 ± 0.4	0.915 ± 0.177
Si	100.0 ± 1.30	100 ± 5	1.000 ± 0.052
P	0.77 ± 0.33	1.05 ± 0.10	0.733 ± 0.322
S	13.1 ± 0.9	49 ± 6	0.267 ± 0.038
Ar	2.23 ± 0.63	10.2 ± 2.6	0.219 ± 0.083
K	0.40 ± 0.34	0.38 ± 0.03	1.053 ± 0.899
Ca	6.01 ± 0.93	6.3 ± 0.3	0.954 ± 0.154
Fe	100.8 ± 1.9	112 ± 29	0.900 ± 0.234
Co	0.19 ± 0.06	0.23 ± 0.02	0.826 ± 0.271
Ni	5.68 ± 0.22	5.0 ± 0.24	1.136 ± 0.070

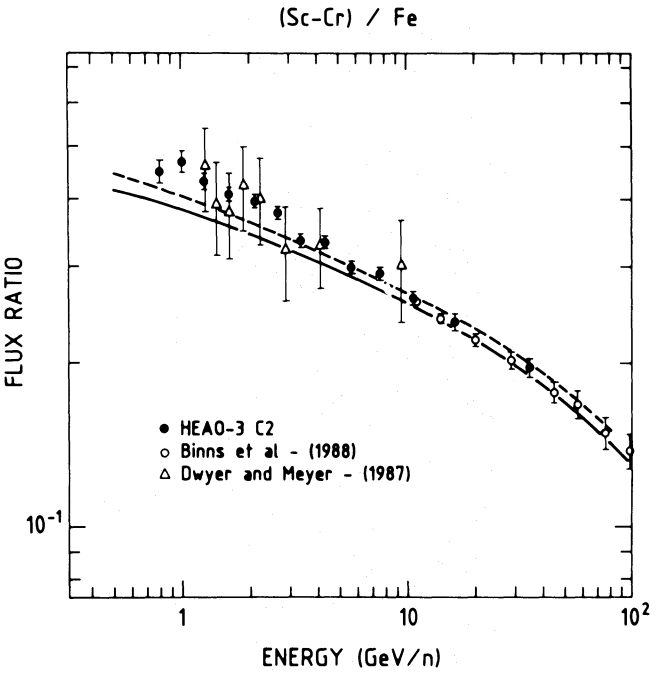

Fig. 16. Predicted and observed (Sc+Ti+V+Cr)/Fe ratio (see Fig. 7 caption). *Continuous curve*: interstellar medium: 90% H, 10% He. *Dashed curve*: interstellar medium: 100% H

were lower by 5%, the Na source abundance would be higher by 23%.

Therefore the differences with our previous cosmic ray source abundances are mainly due to the improvements in the cross section data: we are now using the most recent and exhaustive cross section measurements by the New Hampshire and Saclay groups (Webber, 1987 and ref. therein; Gupta and Webber, 1989; Ferrando et al., 1988b), together with the semi-empirical formula from Webber (1987).

In Table 7, we give the updated ratios of the Galactic Cosmic Ray Source abundances to the Local Galactic abundances taken from Anders and Grevesse (1989). These ratios are clearly correlated with the first ionization potential (FIP), as stressed by many authors (Casse and Goret, 1978; Meyer, 1985b); it is shown on Fig. 18, where a two-step structure is observed with a low FIP plateau below ~ 8.5 eV and a high FIP one. The high FIP elements are underabundant by a factor of 4 to 6, with the remarkable exception of N which is underabundant by a factor of ~ 12.

Compared to the bulk of low FIP elements, Na appears to be low by a factor of ~ 0.55. Na is volatile while the other low FIP

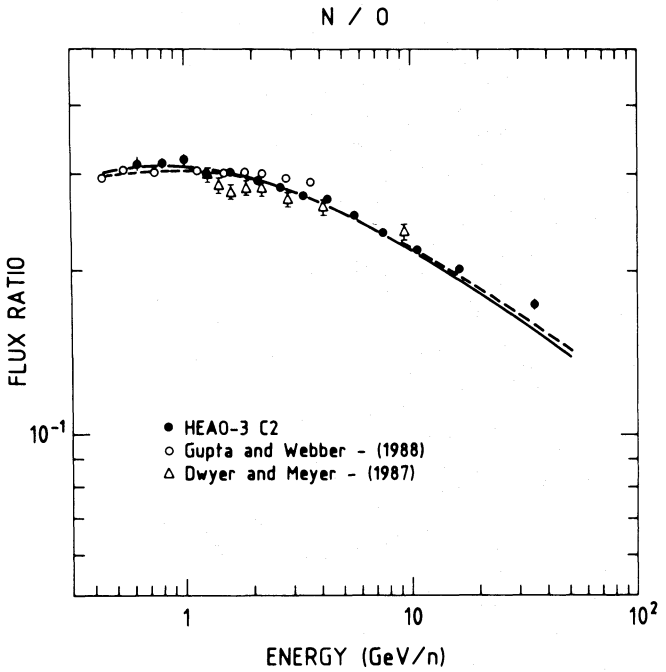

Fig. 17. Observed and calculated N/O ratio (see Fig. 7 caption). *Continuous curve*: predicted ratio for nominal values of the partial cross sections and for a N/O source abundance of 4.8%. *Dashed curve*: predicted ratio for cross section values lower by 5% and for a N/O source abundance of 6.4%

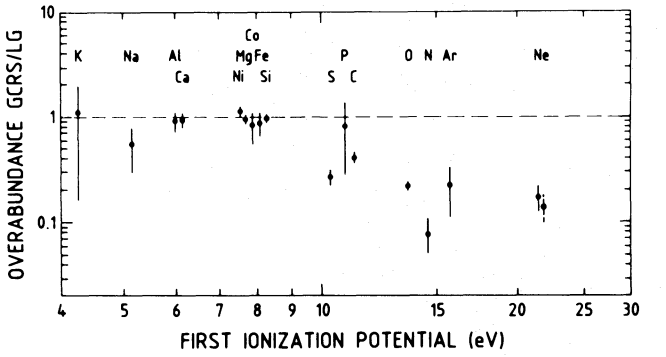

Fig. 18. Overabundance of galactic cosmic ray sources with respect to local galactic composition as a function of first ionization potential. For Ne we give also (dashed) the overabundance for ^{20}Ne, thus excluding the "anomalous" ^{22}Ne component

elements of Table 5 are refractory. This could indicate that volatility plays a role in the selection of ions prior to acceleration. This argument could be strengthened by the observation that Ge and Pb, which belong to the same category of volatile low FIP elements, are also underabundant, as stressed by Meyer (1981, 1985a). But, as shown later by Grevesse and Meyer 1985, it is true if the LG abundance is based on C1 meteoritic values, but no more if based on photospheric values, so the question is still open.

The adjusted nitrogen to oxygen source ratio of $4.83 \pm 1.66\%$, matches reasonably well the energy dependence of the observed N/O ratio (Fig. 17). This value agrees within uncertainties with the value of $6.7 \pm 3.8\%$, obtained from isotopes at ~ 3 GeV/n by Ferrando et al., 1988a, with the value of $3.7 \pm 1.7\%$, obtained from an analysis of low energy isotope data by Krombel and Wiedenbeck, 1988 and with the value of $3.8 \pm 1.0\%$, obtained by Gupta and Webber, 1988 from an analysis of the high and low energy isotope and element data. Although we are using the set of cross sections from the New Hampshire group for secondary production in hydrogen, our calculated N/O source abundance is $\sim 1\%$ higher. As noted above, our new boron to carbon data lies $\sim 4\%$ below the previously reported one between 2 to 5 GeV/n. Our N/O source abundance had to be increased accordingly, making our calculation quite compatible with those of Gupta and Webber. Note that our uncertainty allows a significant deviation of the nitrogen abundance from our nominal value. This can be seen on Fig. 17, where we have also plotted (dashed) the N/O ratio calculated with partial cross section values 5% lower than the nominal ones, and keeping λ_{esc} unchanged. It is seen that a reasonably good agreement is obtained, provided the N/O source ratio is taken $\sim 6.4\%$ instead of 4.8%.

6.3. Source energy spectra

If cosmic rays have been accelerated by shock waves, the expected source energy spectrum should be a power law in momentum (see e.g. Axford, 1981; Ormes and Protheroe, 1983):

$$dQ/dE \propto P^{-\gamma}. \quad (1)$$

Furthermore, the modulation parameter for the period considered is about 500–600 MV (Lockwood and Webber, 1979, 1981). Using the source spectrum (1) and a modulation parameter of 600 MV, we find that a reasonable fit to the oxygen spectrum is obtained with $\gamma = 2.23 \pm 0.02$ up to 16 GeV/n (Fig. 8). But the fit does not extend to the highest energy point. This γ value is somewhat at variance with out previous estimate of 2.41 ± 0.05 (Engelmann et al., 1985). This change is probably due to the different method of analysis used to draw the oxygen spectrum free from geomagnetic effects. We used previously an iteration method to unfold the spectrum, while now we directly get this spectrum by a conservative selection of data (see Sect. 5.1). The extensive checks at each step of the present work make us more confident on the reliability of this new spectral shape.

The γ value we derive below 16 GeV/n is of course slightly dependent on the value chosen for the modulation parameter: a 100 MV error on this value would propagate into a 0.05 error on the γ index of the oxygen spectrum below 10 GeV/n. We therefore adopt for this spectral index:

$$\gamma = 2.23 \pm 0.05$$

Now, we cannot a priori exclude other mathematical description of the source spectral shape, which might provide a better fit of our data up to 35 GeV/n. As an example, we have used earlier (Perron et al., 1981) a power law in total energy E_{tot}:

$$dQ/dE \propto E_{tot}^{-\gamma}. \quad (2)$$

With the formula (2) and a modulation parameter of 500 MV, we find that a good fit to the oxygen and iron spectra is obtained with $\gamma = 2.40 \pm 0.03$ up to 35 GeV/n (dashed in Figs. 11 and 12). These results illustrate the fact that the HEAO-3 data alone do not permit to choose between different spectral shapes. This

determination should wait until we have reliable higher energy data.

If we take the same spectral shape for all elements, we find that the abundance ratios calculated with the propagation program are in relatively good agreement with the experimental values plotted in Figs. 7 and 8. However slight deviations from this law might be present in the Ne and Mg spectra, the Ne spectrum seeming a little flatter (by 0.02 in spectral index) and the Mg spectrum a little steeper than the Si spectrum.

In this derivation of the source spectra, we did not consider a possible truncation of the pathlengths at low energies. If such a truncation is present at low energy, as seemingly indicated by the comparison of the B/C and Sc-Cr/Fe ratios (Fig. 13 and 16), the source spectral shape of all the species heavier than carbon must be slightly steeper than indicated by the leaky box calculation, and this steepening must increase with the charge. Indeed, if for heavier nuclei, higher secondary to primary ratios at low energies are produced by truncation, nuclear destruction must be more effective and result in higher source values as well, in order to account for the observed primary abundance. That truncation effect should not affect the O source spectrum (since it is adjusted to fit the nearby B/C ratio), but may result in an increase of <0.1 in the source spectral index in the iron group.

7. Conclusion

The nuclear composition and the energy spectra of galactic cosmic rays, drawn from HEAO-3 data have already been presented at several cosmic ray conferences. We thought however it would be useful to present in a single paper these results spread in several publications. We took this opportunity to revisit our data and to update the values of some parameters needed in the data analysis, such as the spallation cross sections, including the recently measured He spallation cross sections (Webber et al., 1989; Ferrando et al., 1988b).

The rigidity dependence of the mean escape length we derive in the frame of the leaky box model from the B/C ratio is now:

$\lambda_{esc} = 34.1\ \beta R^{-0.60}\ \mathrm{g\,cm^{-2}}$ for $R > 4.4$ GV

$\lambda_{esc} = 14.0\ \beta\ \mathrm{g\,cm^{-2}}$ for $R < 4.4$ GV

assuming an interplanetary medium composed of 90% of H and 10% of He, with a density of 0.3 atoms $\mathrm{cm^{-3}}$.

By comparison with the law we have previously derived for a medium of pure H (Koch Miramond et al., 1983), the λ_{esc} is increased at all rigidities and the (Sc-Cr)/Fe predicted ratio is decreased, as discussed in Ferrando et al., 1985, 1988b. Some truncation of pathlength may be necessary below 5 GeV/n (Garcia Munoz et al., 1984, 1987). Above 5 GeV/n, all secondary over primary ratios are relatively well fit by the same law for the escape length, so we can use these high energy data to derive the source abundances of all mainly primary nuclei in the frame of the simple leaky box model. When compared to the local galactic (LG) abundances recently published by Anders and Grevesse, 1989, the source abundances show up the classical first ionization potential pattern, extensively described in the literature (e.g. Meyer, 1985b).

As regards the energy spectra of all elements of charge ≥ 4, they have been obtained by a different analysis method from that used previously. By applying very conservative selection criteria, absolute energy spectra could be drawn from the data, without the need of normalization at a given energy with the average published value, as was done previously. From these observed spectra, and assuming a modulation parameter around 550 MV, the source spectra of all elements could be derived in the frame of the leaky box model. A source spectrum in the shape of a power law in momentum, as predicted by the shock wave acceleration theory, can fit the oxygen data only up to 16 GeV/n, with a spectral index of 2.23 ± 0.05. This index is not significantly different from that found for H and He nuclei, showing that, within errors, all elements have the same source spectrum, at least between 1 and 16 GeV/n. The fit for elements of charge ≥ 4 would be extended to higher energy (35 GeV/n), with a source spectrum in the shape of a power law in total energy, the spectral index being then around 2.40. But definite conclusion on this spectral shape should wait for accurate higher energy observations. No significant differences in the source spectral index are observed for the different types of nuclei, except perhaps for Ne and Mg.

Acknowledgements. We are deeply indebted to W.R. Webber for providing us with his updated tables of cross sections, prior to publication. We express also our gratitude to Catherine Cesarsky and Jean-Paul Meyer for many stimulating discussions and suggestions during the preparation of the manuscript.

Appendix A

Procedure adopted to transform an integral energy flux value into a differential flux value.

If the differential energy spectrum of a certain type of particle can be fit by a power law $dJ/dE = KE^{-\gamma}$, the mean energy of the particles above an energy E_0 is:

$E_m = \alpha E_0$ with $\alpha = (\gamma - 1)/(\gamma - 2)$.

Since α is a function of γ, it has different values for different types of particles (as an example, $\alpha = 2.33$ for $\gamma = 2.75$ and $\alpha = 1.8$ for $\gamma = 3.25$).

Now, at which energy should we plot the point corresponding to the abundance ratio of two elements, measured above some energy E_0? We can decide to plot it at an energy $E' = 1.8\,E_0$, as proposed by Juliusson, 1974, and to apply a correction factor to the abundance ratio. This correction factor is computed as follows:

The integral flux above E_0 of the element i with differential spectrum $j_i = k_i E^{-\gamma} i$ is:

$J_i(E_0) = k_i(\gamma_i - 1)^{-1} E_0^{-\gamma_i + 1}$

and the differential flux at the energy $E' = 1.8\,E_0$ is:

$J_i(E') = J_i(E_0)\eta_i / E_0$ with $\eta_i = (\gamma - 1)1.8^{-\gamma}$

η_i varies slowly with γ_i (between 0.35 for $\gamma = 2.75$ and 0.325 for $\gamma = 3.4$). Therefore γ_i should be first roughly estimated before the correction factor η_i can be computed for an element i.

Finally, the differential abundance ratio of two elements i and k at energy $E' = 1.8\,E_0$ is simply given by:

$j_i/j_k = (J_i/J_k)(\eta_i/\eta_k)$

where J_i and J_k are the integral flux values above E_0 for the elements i and k.

References

Anders, E., Grevesse, N.: 1989, *Geochim. Cosmochim. Acta* **53**, 197

Axford, W.I.: 1981, *Proc. 17th Int. Cosmic Ray Conf., Paris* **12**, 155

Benegas, J.C., Israel, M.H., Klarmann, J., Maehl, R.C.: 1975, *Proc. 14th Int. Cosmic Ray Conf., Munchen* **1**, 251

Bouffard, M., Engelmann, J.J., Koch, L., Soutoul, A., Lund, N., Peters, B., Rasmussen, I.L.: 1982, *Astrophys. Space Sci.* **84**, 3

Byrnak, B., Lund, N., Rasmussen, I.L., Rotenberg, M., Engelmann, J.J., Goret, P., Juliusson, E.: 1983, *Proc. 18th Int. Cosmic Ray Conf., Bangalore* **2**, 29

Caldwell, J.H.: 1977, *Astrophys. J.* **218**, 269

Cantin, M., Casse, M., Koch, L., Jouan, R., Mestreau, P., Roussel, D., Bonnin, F., Moutel, J., Teichner, S.J.: 1974, *Nucl. Instr. Meth.* **118**, 177

Cantin, M., Engelmann, J.J., Masse, P., Rotenberg, M.: 1981, *Proc. 17th Int. Cosmic Ray Conf., Paris* **8**, 59

Cassé, M., Goret, P.: 1978, *Astrophys. J.* **221**, 703

Chappell, J.H., Webber, W.R.: 1981, *Proc 17th Int. Cosmic Ray Conf., Paris* **2**, 59

Corydon-Petersen, O., Dayton, B., Lund, N., Melgaard, K., Omo, K., Peters, B., Risbo, T.: 1970, *Nucl. Instr. and Meth.* **81**, 1

Crane, J.H., Israel, M.H., Klarmann, J., Ormes, J.F., Protheroe, R.J.: 1983, *Astrophys. and Space Sci.* **94**, 211

Dwyer, R., Meyer, P.: 1985, *Astrophys. J.* **294**, 441

Dwyer, R., Meyer, P.: 1987, *Astrophys. J.* **322**, 981

Engelmann, J.J., Cantin, M.: 1978, *J. Phys.* **39**, C3-57

Engelmann, J.J., Goret, P., Juliusson, E., Koch-Miramond, L., Masse, P., Petrou, N., Rio, Y., Soutoul, A.: 1981, *Proc. 17th Int. Cosmic Ray Conf., Paris* **9**, 97

Engelmann, J.J., Goret, P., Juliusson, E., Koch-Miramond, L., Masse, P., Soutoul, A., Byrnak, B., Lund, N., Peters, B., Rasmussen, I.L., Rotenberg, M., Westergaard, N.J.: 1983, *Proc. 18th Int. Cosmic Ray Conf., Bangalore* **2**, 17

Engelmann, J.J.: 1984, *9th European Cosmic Ray Symp., Kosice*, eds. K. Kudela, S. Pinter, Slovac Acad. Sci., Moscow p. 141

Engelmann, J.J., Goret, P., Juliusson, E., Koch-Miramond, L., Lund, N., Masse, P., Rasmussen, I.L., Soutoul, A.: 1985, *Astron. Astrophys.* **148**, 12

Fenton, A.G., Fenton, K.B., Humble, J.E.: 1983, *Proc. 18th Int. Cosmic Ray Conf., Bangalore* **10**, 164

Ferrando, P., Engelmann, J.J., Goret, P., Koch-Miramond, L., Petrou, N., Soutoul, A., Herrstrom, N.Y., Byrnak, B., Lund, N., Peters, B., Rasmussen, I.L., Rotenberg, M., Westergaard, N.J.: 1988a, *Astron. Astrophys.* **193**, 69

Ferrando, P., Webber, W.R., Goret, P., Kish, J.C., Schrier, D.A., Soutoul, A., Testard, O.: 1988b, *Phys. Rev. C* **37**, 1490

Garcia-Munoz, M., Mason, G.M., Simpson, J.A., Wefel, J.P.: 1977, *Proc. 15th Int. Cosmic Ray Conf., Plovdiv*, **1**, 230

Garcia-Munoz, M., Simpson, J.A.: 1979, *Proc 16th Int. Cosmic Ray Conf., Kyoto* **1**, 270

Garcia-Munoz, M., Simpson, J.A., Guzik, T.G., Wefel, J.P., Margolis, S.H.: 1987, *Astrophys. J. Suppl.* **64**, 269

Grevesse, N., Meyer, J.P.: 1985, *Proc. 19th Int. Cosmic Ray Conf., La Jolla* **3**, 5

Gupta, M., Webber, W.R.: 1989, *Astrophys. J.* **340**, 1124

Herrström, N.Y., Lund, N.: 1985, *Proc. 19th Int. Cosmic Ray Conf., La Jolla* **2**, 100

Juliusson, E.: 1974, *Astrophys. J.* **191**, 331

Juliusson, E., Engelmann, J.J., Jorrand, J., Koch-Miramond, L., Masse, P., Petrou, N.: 1983, *Proc. 18th Int. Cosmic Ray Conf., Bangalore* **2**, 21

Koch-Miramond, L., Engelmann, J.J., Goret, P., Juliusson, E., Masse, P., Soutoul, A., Perron, C., Lund, N., Rasmussen, I.L.: 1983, *Proc. 18th Int. Cosmic Ray Conf., Bangalore* **9**, 275

Koch-Miramond, L., Meyer, J.P.: 1984, *Adv. Space Res.* **4**, 79

Krombel, K.E., Wiedenbeck, M.E.: 1988, *Astrophys. J.* **328**, 940

Lezniak, J.A., Webber, W.R.: 1978, *Astrophys. J.* **223**, 676

Lockwood, J.A., Webber, W.R.: 1979, *J. Geophys. Res.* **84**, A, 120

Lockwood, J.A., Webber, W.R.: 1981, *Proc. 17th Int. Cosmic Ray Conf., Paris* **3**, 259

Lund, N., Rasmussen, I.L., Rotenberg, M., Masse, P., Engelmann, J.J., Jorrand, J., Petrou, N.: 1981a, *Proc. 17th Int. Cosmic Ray Conf., Paris* **8**, 67

Lund, N., Westergaard, N.J., Engelmann, J.J., Goret, P., Juliusson, E.: 1981b, *Proc. 17th Int. Cosmic Ray Conf., Paris* **8**, 63

Lund, N.: 1984, *Adv. Space Res.* **4**, 5

Lund, N., Rotenberg, M.: 1985, *Proc. 19th Int. Cosmic Ray Conf. La Jolla* **2**, 330

Maehl, R.C., Ormes, J.F., Fisher, A.J., Hagen, F.A.: 1977, *Astrophys. Space Sci.* **47**, 163

Meyer, J.P.: 1981, *Proc. 19th Int. Cosmic Ray Conf., Paris* **2**, 281

Meyer, J.P.: 1985a, *Proc. 17th Int. Cosmic Ray Conf., La Jolla* **9**, 141

Meyer, J.P.: 1985b, *Astrophys. J. Suppl.* **57**, 173

Minagawa, G.: 1981, *Astrophys. J.* **248**, 847

Ormes, J.F., Protheroe, R.J.: 1983, *Astrophys. J.* **272**, 756

Orth, C.D., Buffington, A., Smoot, G.F., Mast, T.S.: 1978, *Astrophys. J.* **226**, 1147

Perron, C., Engelmann, J.J., Goret, P., Juliusson, E., Koch-Miramond, L., Meyer, J.P., Soutoul, A., Lund, N., Rasmussen, I.L., Westergaard, N.: 1981, *Proc. 17th Int. Cosmic Ray Conf., Paris* **9**, 118

Rotenberg, M., Rasmussen, I.L., Engelmann, J.J., Masse, P., Rio, Y.: 1981, *Proc. 17th Int. Cosmic Ray Conf., Paris* **8**, 112

Sato, Y., Shimada, E., Ohta, I., Tasaka, S., Tanaka, S., Sugimoto, H., Taira, K., Tateyama, N.: 1985, *Proc. 19th Int. Cosmic Ray Conf., La Jolla* **2**, 36

Simon, M., Spiegelhauer, H., Schmidt, W., Siohan, F., Ormes, J.F., Balasubrahmanyan, V.K., Arens, J.F.: 1980, *Astrophys. J.* **239**, 712

Soutoul, A., Ferrando, P.: 1989, in "*Cosmic Abundances of Matter*", ed. C.J. Waddington, *AIP Conf. Proc. 183*, American Institute of Physics, New York

Soutoul, A., Ferrando, P., Webber, W.R.: 1990, *Proc. 21th Int. Cosmic Ray Conf., Adelaide*, **3**, 337

Webber, W.R., Damle, S.V., Kish, J.: 1972, *Astrophys. Space Sci.* **15**, 245

Webber, W.R.: 1982, *Astrophys. J.* **255**, 329

Webber, W.R.: 1987, *Proc. 20th Cosmic Ray Conf., Moscow* **2**, 463

Webber, W.R.: 1989, private communication

Webber, W.R., Soutoul, A., Ferrando, P., Gupta, M.: 1990, *Astrophys. J.* **348**, 611

Westfall, G.D., Wilson, L.W., Lindstrom, P.J., Crawford, H.J., Greiner, D.E., Heckman, H.H.: 1979, *Phys. Rev. C* **19**, 1309

Young, J.S., Freier, P.S., Waddington, C.J., Brewster, N.R., Fickle, R.K.: 1981, *Astrophys. J.* **246**, 1014